1

2

3

4 **Iterative Methods for Solving the Nonlinear Balance Equation**

5 **with Optimal Truncation**

6

7

8 Qin XU[1*] and Jie CAO[2,3]

9

10

11 [1]*NOAA/National Severe Storms Laboratory, Norman, Oklahoma, USA*

12 [2]*Cooperative Institute for Mesoscale Meteorological Studies, University of Oklahoma,*

13 *Norman, Oklahoma, USA*

14 [3]*Institute of Atmospheric Physics, Chinese Academy of Sciences, Beijing* 100029

15

16

18

19

20

21

----
* Corresponding author: Qin Xu
E-mail: Qin.Xu@noaa.gov

ABSTRACT

Two types of previous iterative methods for solving the nonlinear balance equation (NBE) are revisited. In the first type, the NBE is rearranged into a linearized equation for a presumably small correction to the initial guess or the subsequent updated solution. In the second type, the NBE is rearranged into a quadratic form of the absolute vorticity with the positive root of this quadratic form used in the form of Poisson equation to solve NBE iteratively. The two methods are re-derived by expanding the solution asymptotically upon a small Rossby number, and a criterion for optimally truncating the asymptotic expansion is proposed to obtain the super-asymptotic approximation of the solution. For each re-derived method, two iterative procedures are designed using the integral-form Poisson solver versus the over-relaxation scheme to solve the boundary value problem in each iteration. Tested with analytically formulated wavering jet flows on the synoptic, sub-synoptic and meso-α scales, the iterative procedure designed for the first method with the Poisson solver, named M1a, is found to be the most accurate and efficient. For the synoptic wavering jet flow in which the NBE is entirely elliptic, M1a is extremely accurate. For the sub-synoptic wavering jet flow in which the NBE is mostly elliptic, M1a is sufficiently accurate. For the meso-α wavering jet flow in which the NBE is partially hyperbolic so its boundary value problem becomes seriously ill-posed, M1a can effectively reduce the solution error for the cyclonically curved part of the wavering jet flow but not for the anti-cyclonically curved part.

Keywords: nonlinear balance, iterative method, optimal truncation

43

Article Highlights:

- Two previous iterative methods for solving the NBE are re-derived by expanding the solution asymptotically upon a small Rossby number Ro.

- A criterion for optimal truncation of asymptotic expansion is proposed to obtain the super-asymptotic approximation of the solution.

- Using the integral-form Poisson solver for the boundary value problem in each iteration, optimally truncated solutions can be obtained efficiently with improved accuracies.

- Solution errors can be reduced effectively even when Ro increases to 0.4 for cyclonically curved jet flows of meso-α scale.

1. Introduction

For flows of synoptic and sub-synoptic scales in the middle and high latitudes, the nonlinear balance equation (NBE) links the streamfunction field with the geopotential field more accurately than the geostrophic balance (Charney, 1955; Bolin, 1955). However, solving the streamfunction from the NBE for a given geopotential field can be very challenging due to complicated issues on the existence of solution in conjunction with difficulties caused by nonlinearity (Courant and Hilbert, 1962). It is well known mathematically that the NBE is a special case of the Monge-Ampere differential equation for the streamfunction (Charney, 1955). If the geostrophic vorticity (that is, the vorticiy of geostrophic flow associated with the given geopotential field) is larger than $-f/2$ for a constant f where f is the Coriolis parameter, then the NBE is of the elliptic type and its associated boundary value problem can have no more than two solutions (see Section 6.3 in Chapter 4 of Courant and Hilbert, 1962). If the geostrophic vorticity is smaller than $-f/2$ in a local area, then the NBE becomes locally hyperbolic. In this case, the boundary value problem becomes ill-posed and thus may have no solution although the NBE can be integrated along the characteristic lines within the locally hyperbolic area (see Section 3 of Appendix I in Chapter 5 of Courant and Hilbert, 1962).

To avoid the complication and difficulties caused by the local non-ellipticity in solving the NBE, one can simply enforce the ellipticity condition to a certain extent by slightly smoothing or adjusting the given geopotential field. This type of treatment has been commonly used in previously developed iterative methods to solve the NBE as a boundary value problem (Bolin, 1955, 1956; Shuman, 1955, 1957; Miyakoda, 1956; Bushby and Huckle, 1956; Arnason, 1958;

4

76   Bring and Charasch, 1958; Liao and Chow, 1962; Asselin, 1967; Paegle and Tomlinson, 1975;

77   Bijlsma and Hoogendoorn, 1983). However, regardless of the above treatment, the convergence

78   properties of the previous iterative methods or any iterative methods can be not only scale-

79   dependent but also flow-dependent and thus very difficult to study theoretically and rigorously.

80   The above reviewed previous iterative methods can be classified into two types. In the first

81   type (originally proposed by Bolin, 1955), the NBE is transformed into a linearized equation

82   for a presumably small correction to the initial guess or to the subsequent updated solution

83   when this linearized equation is solved iteratively. In the second type (originally proposed by

84   Shuman, 1955, 1957; Miyakoda, 1956), the NBE is rearranged into a quadratic form of the

85   absolute vorticity and the positive root of this quadratic form is used in the form of Poisson

86   equation to solve for the streamfunction iteratively. The initial guess for both types is the

87   geostrophic streamfunction. Their convergence properties were analyzed theoretically, but the

88   analysis was lack of rigor and generality, because the coefficients of linearized differential

89   operator for the first type and the forcing terms on the right-hand side of the iterative form of

90   linearized equation for the second type were functions of space but treated as constants

91   (Arnason, 1958; Bijlsma and Hoogendoorn, 1983). Therefore the convergence properties of the

92   previously iterative methods were examined mainly through numerical experiments. Besides,

93   due to the very limited computer memories and speed in those early decades, the previous

94   iterative methods employed the memory-saving sequential relaxation scheme based on the

95   classical Liebmann-type iteration algorithm (Southwell, 1946) and applied to coarse resolution

96   grids for large-scale flows. The sequential relaxation and successive over-relaxation (SOR)

97	schemes have been used in the second type of iterative method (Shuman, 1955, 1957) to solve

98	the NBE for hurricane flows (Zhu et al., 2002). However, using the previous iterative methods

99	to solve the NBE still faces various difficulties especially when the spatial scale reduces to and

100	even below the sub-synoptic scale. In particular, there are unaddressed challenging issues

101	concerning whether and how the solutions can be obtained approximately and efficiently

102	through limited numbers of iterations, especially when the NBE becomes locally hyperbolic

103	(due mainly to reduced spatial scales) and thus the iterative methods fail to converge.

104	 This paper aims to address the above concerned challenging issues. In particular, we will

105	re-derive the above two types of iterative methods formally and systematically by expanding

106	the solution asymptotically upon a small Rossby number and substituting it into the NBE. Since

107	the asymptotic expansion is not ensured to converge especially when the Rossby number is not

108	sufficiently small, the concept of optimal truncation of asymptotic expansion is employed and

109	a criterion is proposed for optimal truncation to obtain the super-asymptotic approximation of

110	the solution based on the heuristic theory of asymptotic analysis (Boyd, 1999). As will be seen

111	in this paper, by employing the optimal truncation, the issue on non-convergence of the iterative

112	methods caused by the increase of Rossby number can be addressed to a certain extent. Besides,

113	the recently developed Poisson solver based on integral formulas (Xu et al., 2011; Cao and Xu,

114	2011) will be used in comparison with the aforementioned classical SOR scheme to solve the

115	boundary value problem in each iterative step. In particular, for flows of sub-synoptic scale or

116	meso-α scale, the NBE can become locally hyperbolic and the solution will be checked in this

117	paper via the proposed optimal truncation under certain conditions.

118   The paper is organized as follows. The next section presents formal and systematical

119   derivations of the above reviewed two iterative methods. Section 2 formulates the criterion for

120   optimal truncation, and section 3 constructs four different iterative procedures with optimal

121   truncation and designs numerical experiments for testing the iterative procedures. Section 4

122   examines and compares the results of experiments performed with the four iterative procedures,

123   followed by conclusions in section 5.

124

125   **2. Derivations of two iterative methods**

126   *2.1 Scaling and asymptotic expansion based on small Rossby number*

127   The NBE can be written into the following form (Charney, 1955):

128

129    $\quad N(\psi) = \nabla^2 \phi,$ (1a)

130

131   where $N(\psi) \equiv \nabla^2 \psi + (\nabla \psi)\cdot\nabla f + 2J_{xy}(\partial_x \psi, \partial_y \psi) = \nabla\cdot(f\nabla \psi) + 2J_{xy}(\partial_x \psi, \partial_y \psi) = \nabla^2(f\psi) - \nabla\cdot(\psi\nabla f)$

132    $+ 2J_{xy}(\partial_x \psi, \partial_y \psi)$, ψ is the streamfunction, ϕ is the geopotential, $\nabla \equiv (\partial_x, \partial_y)$, $\nabla^2 \equiv \nabla\cdot\nabla = \partial_x^2 +$

133   ∂_y^2, and $J_{xy}(\partial_x \psi, \partial_y \psi) \equiv (\partial_x^2 \psi)(\partial_y^2 \psi) - (\partial_x\partial_y \psi)^2$. For large-scale and synoptic-scale flows, the

134   geostrophic approximation, $\nabla^2 \phi \approx \nabla^2(f\psi)$, is the leading-order balance in (1a) and thus $\nabla^2(f\psi)$

135   is the dominant term in $N(\psi)$. In this case, the boundary condition for solving ψ from (1a) over

136   a middle-latitude domain D can be given by

137

138    $\quad \psi = \psi_g \quad$ on $\partial D,$ (1b)

139

140   where ∂D denotes the domain boundary, and $\psi_g \equiv \phi/f$ is the global geostrophic streamfunction

7

141   (Kuo, 1959; Charney and Stern, 1962; Schubert et al., 2009).

142   Formally, we can scale x and y by L, scale $f = f_o + f'$ by f_o, and scale ψ and ϕ by UL and

143   f_oUL, respectively, where U is the horizontal velocity scale, L is the horizontal length scale, f_o

144   is a constant reference value of f which can be the value of f at the domain center. The scaled

145   variables are still denoted by their respectively original symbols, so the NBE can have the

146   following non-dimensional form:

147

148    $\qquad \nabla^2(f\psi - \phi) = \nabla\cdot(\psi\nabla f') - R_o 2J_{xy}(\partial_x\psi, \partial_y\psi),$ (2)

149

150   where $R_o \equiv U/f_oL$ is the Rossby number. For synoptic-scale and sub-synoptic-scale flows, the

151   above scaling can give $R_o = \varepsilon < 1$. Substituting this into (2) gives

152

153    $\qquad \nabla^2(f\psi - \phi) = \varepsilon[\nabla\cdot(\psi\nabla F) - 2J_{xy}(\partial_x\psi, \partial_y\psi)],$ (3)

154

155   where $F = f'/(f_oR_o) \leq O(1)$ and O( ) is the 'order-of-magnitude' symbol. Thus, ψ can have the

156   following asymptotic expansion:

157

158    $\qquad \psi = \psi_0 + \sum_1 \varepsilon^k \delta\psi_k,$ (4)

159

160   where $\psi_0 = \psi_g$ and $\sum_1$ denotes the summation over k from 1 to ∞. The kth order truncation of

161   the asymptotic expansion of ψ in (4) is given by $\psi_k \equiv \psi_0 + \sum_1^k \varepsilon^{k'} \delta\psi_{k'}$, where $\sum_1^k$ denotes the

162   summation over k' from 1 to k. Formally, $\psi = \psi_k + O(\varepsilon^{k+1})$, so ψ_k is accurate up to $O(\varepsilon^k)$ as an

163   approximation of ψ.

164   By substituting (4) into (3) and (1b), and then collecting terms of the same order of ε, we

8

165 obtain

166

167 $$\nabla^2(f\delta\psi_1) = \nabla\cdot(\psi_0\nabla F) - 2J_{xy}(\partial_x\psi_0, \partial_y\psi_0),$$

168 $$\nabla^2(f\delta\psi_2) = \nabla\cdot(\delta\psi_1\nabla F) - 2[J_{xy}(\partial_x\psi_0, \partial_y\delta\psi_1) + J_{xy}(\partial_x\delta\psi_1, \partial_y\psi_0)],$$

169 $$\nabla^2(f\delta\psi_3) = \nabla\cdot(\delta\psi_2\nabla F) - 2[J_{xy}(\partial_x\psi_0, \partial_y\delta\psi_2) + J_{xy}(\partial_x\delta\psi_2, \partial_y\psi_0) + J_{xy}(\partial_x\delta\psi_1, \partial_y\delta\psi_1)],$$

170 $$\nabla^2(f\delta\psi_4) = \nabla\cdot(\delta\psi_3\nabla F) - 2[J_{xy}(\partial_x\psi_0, \partial_y\delta\psi_3) + J_{xy}(\partial_x\delta\psi_3, \partial_y\psi_0)$$

171 $$+ J_{xy}(\partial_x\delta\psi_1, \partial_y\delta\psi_2) + J_{xy}(\partial_x\delta\psi_2, \partial_y\delta\psi_1)],$$

172 …

173 $$\nabla^2(f\delta\psi_{k+1}) = \nabla\cdot(\delta\psi_k\nabla F) - 2[J_{xy}(\partial_x\psi_0, \partial_y\delta\psi_k) + J_{xy}(\partial_x\delta\delta\psi_k, \partial_y\psi_0) + J_{xy}(\partial_x\delta\psi_1, \partial_y\delta\psi_{k-1})$$

174 $$+ J_{xy}(\partial_x\delta\psi_{k-1}, \partial_y\delta\psi_1) + J_{xy}(\partial_x\delta\psi_2, \partial_y\delta\psi_{k-2}) + J_{xy}(\partial_x\delta\psi_{k-2}, \partial_y\delta\psi_2) + \ldots],$$

175 ... (5a)

176 $$\delta\psi_k = 0 \text{ on } \partial D \text{ for } k = 1, 2, 3, \ldots \qquad (5b)$$

177

178 Here, (5) gives a formal series of linearized equations and boundary conditions for computing

179 $\delta\psi_k$ consecutively from $\delta\psi_1$ to increasingly higher-order term in the expansion of ψ in (5). The

180 equations in (5a), however, are inconvenient to use, because the equation at each given order

181 becomes increasingly complex as the order k increases. It is thus desirable to modify (5a) into

182 a recursive form, and this can be done non-uniquely by first combining the equations in (5a)

183 with $\nabla^2(f\psi_0) = \nabla^2\phi$ into a series of equations for ψ_k (instead of $\delta\psi_k$) and then adding properly

184 selected higher-order terms to the equation for ψ_k at each order without affecting the order of

185 accuracy of the equation. In particular, two different modifications will be made in the next

186 two subsections. From these two modifications, the two types of iterative methods reviewed in

9

187 the introduction for solving the NBE can be derived formally and systematically via the

188 asymptotic expansion of ψ in (4).

189

190 ## 2.2 Derivation of method-1

191 The equations in (5a) can be combined with $\nabla^2(f\psi_0) = \nabla^2\phi$ at $O(\varepsilon^0)$ into a series of equations

192 for ψ_k defined in (4) as shown blow:

193

194 $\nabla^2(f\psi_1) = \nabla^2\phi + \varepsilon\nabla\cdot(\psi_0\nabla F) - 2\varepsilon J_{xy}(\partial_x\psi_0, \partial_y\psi_0),$

195 $\nabla^2(f\psi_2) = \nabla^2\phi + \varepsilon\nabla\cdot(\psi_1\nabla F) - 2\varepsilon[J_{xy}(\partial_x\psi_0, \partial_y\psi_0) + \varepsilon J_{xy}(\partial_x\psi_0, \partial_y\delta\psi_1) + \varepsilon J_{xy}(\partial_x\delta\psi_1, \partial_y\psi_0)]$

196 $= \nabla^2\phi + \varepsilon\nabla\cdot(\psi_1\nabla F) - 2\varepsilon[J_{xy}(\partial_x\psi_1, \partial_y\psi_1) - \varepsilon^2 J_{xy}(\partial_x\delta\psi_1, \partial_y\delta\psi_1)]$

197 $= \nabla^2\phi + \varepsilon\nabla\cdot(\psi_1\nabla F) - \varepsilon 2 J_{xy}(\partial_x\psi_1, \partial_y\psi_1) + O(\varepsilon^3),$

198 $\nabla^2(f\psi_3) = \nabla^2\phi + \varepsilon\nabla\cdot(\psi_2\nabla F) - 2\varepsilon[J_{xy}(\partial_x\psi_1, \partial_y\psi_1) + \varepsilon^2 J_{xy}(\partial_x\psi_0, \partial_y\delta\psi_2) + \varepsilon^2 J_{xy}(\partial_x\delta\psi_2, \partial_y\psi_0)]$

199 $= \nabla^2\phi + \varepsilon\nabla\cdot(\psi_2\nabla F) - 2\varepsilon[J_{xy}(\partial_x\psi_1, \partial_y\psi_1) + \varepsilon^2 J_{xy}(\partial_x\psi_1, \partial_y\delta\psi_2) + \varepsilon^2 J_{xy}(\partial_x\delta\psi_2, \partial_y\psi_1)$

200 $- \varepsilon^3 J_{xy}(\partial_x\delta\psi_1, \partial_y\delta\psi_2) - \varepsilon^3 J_{xy}(\partial_x\delta\psi_2, \partial_y\delta\psi_1)]$

201 $= \nabla^2\phi + \varepsilon\nabla\cdot(\psi_2\nabla F) - 2\varepsilon[J_{xy}(\partial_x\psi_2, \partial_y\psi_2) - \varepsilon^3 J_{xy}(\partial_x\delta\psi_1, \partial_y\delta\psi_2) - \varepsilon^3 J_{xy}(\partial_x\delta\psi_2, \partial_y\delta\psi_1)$

202 $- \varepsilon^4 J_{xy}(\partial_x\delta\psi_2, \partial_y\delta\psi_2)]$

203 $= \nabla^2\phi + \varepsilon\nabla\cdot(\psi_2\nabla F) - 2\varepsilon J_{xy}(\partial_x\psi_2, \partial_y\psi_2) + O(\varepsilon^4),$

204 …

205 $\nabla^2(f\psi_k) = \nabla^2\phi + \varepsilon\nabla\cdot(\psi_{k-1}\nabla F) - 2\varepsilon J_{xy}(\partial_x\psi_{k-1}, \partial_y\psi_{k-1}) + O(\varepsilon^{k+1}),$

206 … (6)

207

208 Formally ψ_k is accurate up to $O(\varepsilon^k)$ and so is $\nabla^2(f\psi_k)$ on the left-hand side of the above k^{th}

209 equation. This implies that the kth equation is accurate only up to $O(\varepsilon^k)$, so the last term $O(\varepsilon^{k+1})$

10

210 (that represents all the high-order terms) on the right-hand side can be neglected without

211 degrading the order of accuracy of the equation. This leads to the following recursive form of

212 equation and boundary condition for solving the NBE iteratively:

213

214 $\quad\quad \nabla^2(f\psi_k) = \nabla^2\phi + \varepsilon\nabla\cdot(\psi_{k-1}\nabla F) - 2\varepsilon J_{xy}(\partial_x\psi_{k-1}, \partial_y\psi_{k-1}),$ (7a)

215 $\quad\quad \psi_k = \psi_g \quad$ on $\partial D \quad$ for $k = 1, 2, 3, \ldots$ (7b)

216

217 If ε is sufficiently small to ensure the convergence of the asymptotic expansion in (5), then ψ_k

218 $\to \psi$ gives the solution of the NBE in the limit of $k \to \infty$.

219 $\quad\quad$ Substituting $\varepsilon\nabla F = \nabla f/f_o$ and $\varepsilon = R_o \equiv U/f_o L$ into (7) gives the dimensional form of (7):

220

221 $\quad\quad \nabla^2(f\psi_k) = \nabla^2\phi + \nabla\cdot(\psi_{k-1}\nabla f) - 2J_{xy}(\partial_x\psi_{k-1}, \partial_y\psi_{k-1}),$ (8a)

222 $\quad\quad \psi_k = \psi_g \quad$ on $\partial D.$ (8b)

223

224 For $f = $ constant, (8a) recovers (5) of Bushby and Huckle (1956), but this recursive form of

225 equation is derived here formally and systematically via the asymptotic expansion of the

226 solution in (4). Substituting the dimensional form of $\psi_k = \psi_{k-1} + \varepsilon^k\delta\psi_k$, that is, $\psi_k = \psi_{k-1} + \delta\psi_k$

227 into (8) gives

228

229 $\quad\quad \nabla^2(f\delta\psi_k) = \nabla^2\phi - N(\psi_{k-1}),$ (9a)

230 $\quad\quad \delta\psi_k = 0$ on ∂D for $k = 1, 2, 3, \ldots$ (9b)

231

232 where $N(\ )$ is the nonlinear differential operator defined in (1a). Analytically, (9a) is identical

233 to (8a) but expressed in an incremental form. Numerically, however, solving $\delta\psi_k$ from (9) and

234 updating ψ_{k-1} to $\psi_k = \psi_{k-1} + \delta\psi_k$ iteratively does not give exactly the same solution as that

235 obtained by solving ψ_k from (8) iteratively. According to our additional numerical experiments

236 (not shown), the solutions obtained from (8) are less accurate (by about an order of magnitude

237 for the case of $R_o = 0.1$) than their counterpart solutions obtained from (9), so the non-

238 incremental form of boundary value problem in (8) will not be considered in this paper.

239

240 ### *2.3 Derivation of method-2*

241 The equation for ψ_k in (7) can be multiplied by 2 and rewritten into

242

243 $$2f\nabla^2\psi_k = 2\nabla^2\phi - 2\varepsilon(\nabla F)\cdot\nabla\psi_{k-1} - 4\varepsilon J_{xy}(\partial_x\psi_{k-1}, \partial_y\psi_{k-1}) + O(\varepsilon^{k+1}), \quad (10)$$

244

245 where $\psi_k = \psi_{k-1} + \varepsilon^k\delta\psi_k = \psi_{k-1} + O(\varepsilon^k)$ and $\nabla^2(f\psi_k) = f\zeta_k + (\nabla f)\cdot\nabla\psi_k + \nabla\cdot(\psi_k\nabla f) = f\zeta_k +$

246 $\varepsilon(\nabla F)\cdot\nabla\psi_k + \varepsilon\nabla\cdot(\psi_k\nabla F) = f\zeta_k + \varepsilon(\nabla F)\cdot(\nabla\psi_{k-1}) + \varepsilon\nabla\cdot(\psi_{k-1}\nabla F) + O(\varepsilon^{k+1})$ are used. One can verify

247 that $-4\varepsilon J_{xy}(\partial_x\psi_k, \partial_y\psi_k) = \varepsilon(\zeta_k^2 - A_k^2 - B_k^2) = \varepsilon\zeta_k^2 - \varepsilon(A_{k-1}^2 + B_{k-1}^2) + O(\varepsilon^{k+1})$ where $\zeta_k = \nabla^2\psi_k$, A_k

248 $\equiv (\partial_x^2 - \partial_y^2)\psi_k$, $B_k \equiv 2\partial_x\partial_y\psi_k$, and $A_k = (\partial_x^2 - \partial_y^2)(\psi_{k-1} + \varepsilon^k\delta\psi_k) = A_{k-1} + O(\varepsilon^k)$ and $B_k = 2\partial_x\partial_y(\psi_{k-}$

249 $_1 + \varepsilon^k\delta\psi_k) = B_{k-1} + O(\varepsilon^k)$ are used. Substituting these into (10) gives

250

251 $$\varepsilon\zeta_k^2 + 2f\zeta_k + 2\varepsilon(\nabla F)\cdot\nabla\psi_{k-1} - 2\nabla^2\phi - \varepsilon A_{k-1}^2 - \varepsilon B_{k-1}^2 = O(\varepsilon^{k+1}).$$

252

253 This leads to the following recursive form of equation that is accurate up to $O(\varepsilon^k)$:

254

255 $$\varepsilon\zeta_k^2 + 2f\zeta_k + 2\varepsilon(\nabla F)\cdot\nabla\psi_{k-1} - 2\nabla^2\phi - \varepsilon A_{k-1}^2 - \varepsilon B_{k-1}^2 = 0. \quad (11a)$$

256

257 Substituting $\varepsilon\nabla F = \nabla f/f_o$ and $\varepsilon = R_o \equiv U/f_oL$ into (11a) gives its dimensional form which

258 can be rewritten into

259

260    $(f + \zeta_k)^2 = M_{k-1} \equiv f^2 + 2\nabla^2 \phi + A_{k-1}^2 + B_{k-1}^2 - 2(\nabla f) \cdot \nabla \psi_{k-1}.$ (11b)

261

262 The non-negative condition of $(f + \zeta_k)^2 \geq 0$ requires $M_{k-1} \geq 0$ on the right-hand side of (11b).

263 Also, as a quadratic equation of $f + \zeta_k$ for given ϕ and ψ_{k-1}, (11b) has two roots, but only the

264 positive root, given by $f + \zeta_k = M_{k-1}^{1/2}$, is physically acceptable (because $f + \zeta_k \geq 0$ is required

265 for stably balanced flow). This leads to the following recursive form of equation and boundary

266 condition for solving the NBE iteratively:

267

268    $\nabla^2 \psi_k = -f + M_{k-1}^{1/2},$ (12a)

269    $\psi_k = \psi_g$ on ∂D for $k = 1, 2, 3, \ldots.$ (12b)

270

271 where $M_{k-1} \geq 0$ is ensured by setting $M_{k-1} = 0$ when the computed M_{k-1} from the previous step

272 becomes negative. Here, (12a) gives essentially the same recursive form of equation as that in

273 (8) of Shuman (1957) for solving the NBE iteratively, but this recursive form of equation is

274 derived here via the asymptotic expansion of the solution in (4).

275

276 **3. Iterative procedures with optimal truncation and experiment design**

277 *3.1 Criterion for optimal truncation*

278   When the Rossby number is not sufficiently small to ensure the convergence of the

279 asymptotic expansion, the optimal truncation of the asymptotic expansion of ψ in (4) can be

280 determined (Boyd, 1999) by an empirical criterion in the following dimensional form:

13

281

$$E[N(\psi_K)] = \min E[N(\psi_k)] \text{ for } k = K, K \pm 1, \dots K \pm m, \tag{13}$$

283

284 where $N(\ )$ is the function form defined in (1a), K is the number of optimal truncation, $E[N(\psi_k)]$

285 $\equiv \|\varepsilon[N(\psi_k)]\|'$, $\|\ \|'$ denotes the root-mean-square (RMS) of discretized field of the variable

286 inside $\|\ \|'$ computed over all the interior grid points (excluding the boundary points) of domain

287 D, and $\varepsilon[N(\psi_k)] \equiv [N(\psi_k) - N(\psi_t)]/\|N(\psi_t)\|' = [N(\psi_k) - \nabla^2\phi]/\|\nabla^2\phi\|'$ is the relative error of $N(\psi_k)$

288 with respect to $N(\psi_t)$ which is also the normalized (by $\|\nabla^2\phi\|'$) residual error of the NBE caused

289 by the approximation of $\psi \approx \psi_k$, and ψ_t denotes the true solution. Here, $E[N(\psi_K)]$ is expected

290 to be the global minimum of $E[N(\psi_k)]$. If $E[N(\psi_k)]$ does not oscillate as k increases, then it is

291 sufficient to set $m = 1$ in (13). Otherwise, m should be sufficiently large to ensure $E[N(\psi_K)]$ be

292 the global minimum of $E[N(\psi_k)]$.

293

294 ***3.2 Iterative procedures***

295   The iterative procedure for method-1 performs the following steps:

296 1. Start from $k = 0$ and set $\psi_0 = \psi_g \equiv \phi/f$ in D and ∂D.

297 2. Substitute ψ_{k-1} (= ψ_0 for $k = 1$) into $N(\psi_{k-1})$ to compute the right-hand-side of (9a), and then

298 solve the boundary value problem in (9) for $\delta\psi_k$.

299 3. Substitute $\psi_k = \psi_{k-1} + \alpha\delta\psi_k$ into $\|N(\psi_k) - \nabla^2\phi\|'$ and save the computed $\|N(\psi_k) - \nabla^2\phi\|'$ where

300   α is an adjustable parameter in the range of $0 < \alpha \leq 1$.

301 4. If $k \geq 2m$, then find $\min\|N(\psi_{k'}) - \nabla^2\phi\|'$, say at $k' = K'$, for $k' = k, k - 1, \dots k - 2m$. If $K' < k -$

302   m, then $K = K'$ and ψ_K gives the optimally truncated solution – the final solution that ends the

303   iteration. Otherwise, go back to step 2.

304   When the Poisson solver (or SOR scheme) is used to solve boundary value problem in the

305   above step 2, the iterative procedure designed for method-1 is named M1a (or M1b). For the

306   Poisson solver used in this paper, the internally induced solution is obtained by using the

307   scheme S2 described in section 2.1 of Cao and Xu (2011) and the externally induced solution

308   obtained by using the Cauchy integral method described in section 4.1 of Cao and Xu (2011).

309   For M1a with $Ro < 0.4$ (or $Ro = 0.4$), it is sufficient to set $m = 1$ and $\alpha = 1$ (or 1/2). For M1b,

310   it is sufficient to set $m = 3$ and $\alpha = 1$.

311   The iterative procedure for method-2 performs the following steps:

312   1. Start from $k = 0$ and set $\psi_0 = \psi_g \equiv \phi/f$ in D and ∂D.

313   2. Substitute ψ_{k-1} into M_{k-1} defined in (11b) to compute the right-hand-side of (12a), and then

314   solve the boundary value problem in (12) for ψ_k.

315   3. Compute and save $\|N(\psi_k) - \nabla^2\phi\|'$.

316   4. Perform this step as described above for step 4 of method-1.

317   When the Poisson solver (or SOR scheme) is used to solve boundary value problem in the

318   above step 2, the iterative procedure designed for method-2 is named M2a (or M2b). For M2a

319   and M2b, it is sufficient to set $m = 1$ and $\alpha = 1$.

320

321   *3.3 Experiment design*

322   To examine and compare the accuracies and computational efficiencies of the four iterative

323   procedures, the true streamfunction field is formulated for a wavering jet flow by

324

325        $\psi_t = -0.5ULtanh[2y/L + 0.5\cos(\pi x'/L)]$ (14)

15

326

327   and the associated velocity components are given by

328

329          $u_t \equiv -\partial_y \psi_t = U\text{sech}^2[2y/L + 0.5\cos(\pi x'/L)]$ (15a)

330   and $v_t \equiv \partial_x \psi_t = 0.25\pi U\sin(\pi x'/L)\text{sech}^2[2y/L + 0.5\cos(\pi x'/L)],$ (15b)

331

332   where $U = 20$ ms^{-1} is the maximum zonal speed of the wavering jet flow, $y = -0.25L\cos(\pi x'/L)$

333   is the longitudinal location (in y-coordinate) of the wavering jet axis as a function of $x' = x$

334   - x_0, and x_0 is the zonal location of wave ridge. By setting the half-wavelength L to 2000, 1000

335   and 500 km, the flow fields formulated in (14) and (15) resemble wavering westerly jet flows

336   on the synoptic, sub-synoptic and meso-α scales, respectively (as often observed on northern-

337   hemisphere mid-latitude 500 hPa weather maps).

338   Four sets of experiments are designed to test and compare the iterative procedures with ψ_t

339   given in (14) over a square domain of $D \equiv [-L \leq x \leq L, -L \leq y \leq L]$. The first set consists of four

340   experiments to test the four iterative procedures (that is, M1a, M1b, M2a and M2b) on the

341   synoptic scale by setting $L = 2000$ km and $x_0 = 0$ for ψ_t in (14). The second set also consists of

342   four experiments but to test the four iterative procedures on the sub-synoptic scale by setting L

343   = 1000 km and $x_0 = 0$ for ψ_t in (14). The third (or fourth) set still consists of four experiments

344   to test the four iterative procedures on the meso-α scale by setting $L = 500$ km and $x_0 = 0$ (or

345   L) for ψ_t in (14). Note that setting $x_0 = 0$ (or L) places the ridge (or trough) of the wavering jet

346   in the middle of domain D, so the nonlinearly balanced flow used for the tests in the third (or

347   fourth) set is curved anti-cyclonically (or cyclonically) in the middle of domain D. For

348   simplicity, the Coriolis parameter f is assumed to be constant and set to $f = f_0 = 10^{-4}$ s^{-1} in all

349   the experiments. The Rossby number, defined by $Ro = U/f_oL$, is thus 0.1, 0.2 and 0.4 for $L =$

350   2000, 1000 and 500 km, respectively.

351   The true geopotential field, ϕ, is obtained by solving the Poisson equation, $\nabla^2\phi = N(\psi_t)$,

352   numerically on a 51×51 grid over domain D with the boundary condition given by $\phi = f\psi_t$. In

353   this case, ψ_t in (14) is also discretized on the same 51×51 grid over the same square domain,

354   and is used to compute the right-hand side of $\nabla^2\phi = N(\psi_t)$ via standard finite-differencing. Then,

355   ϕ is solved numerically by using the Poisson solver of Cao and Xu (2011). The SOR scheme

356   can be also used to solve for ϕ, but the solution is generally less accurate than that obtained by

357   using the Poisson solver. The NBE discretization error (scaled by $||\nabla^2\phi||'$) can be denoted and

358   defined by

359

360        $E(\nabla^2\phi) \equiv ||\nabla^2\phi - N(\psi_t)||'/||\nabla^2\phi||'.$ (16)

361

362   This error is 3.25×10^{-3} (or 4.33×10^{-3}) for ϕ obtained by using the Poisson solver with $L = 2000$

363   (or 1000) but increases to 5.58×10^{-3} (or 5.78×10^{-3}) for ϕ obtained by using the SOR scheme.

364   Thus, the solution obtained by using the Poisson solver is used as the input field of ϕ in the

365   NBE to test the iterative procedures in each set of experiments.

366

367   **4. Results of experiments**

368   *4.1 Results from first set of experiments*

369   For this set of experiments, ψ_t and (u_t, v_t) are plotted in Fig. 1a, ψ_g and $(u_g, v_g) \equiv (-\partial_y\psi_g,$

370    $\partial_x\psi_g)$ are plotted in Fig. 1b, the vorticity $\zeta_t \equiv \nabla^2\psi_t$ is plotted in Fig. 1c, and the geostrophic

17

371 vorticity $\zeta_g \equiv \nabla^2 \psi_g$ is plotted in Fig. 1d. Figure 1c shows that the absolute voticity, defined by

372 $f + \zeta_t$, is positive everywhere so the nonlinearly balanced wavering jet flow is inertially stable

373 over the entire domain (see the proof in Appendix C of Xu, 1994). Figure 1c shows that the

374 geostrophic vorticity ζ_g is larger than $-f/2$ ($= -f_o/2$) everywhere, so the NBE is elliptic over the

375 entire domain and its associated boundary value problem in (1) is well posed.

376   The relative error of ψ_k with respect to ψ_t can be denoted and defined by

377

378      $\varepsilon(\psi_k) \equiv (\psi_k - \psi_t)/\|\psi_t\|,$ (17)

379

380 where $\|\ \|$ denotes the RMS of discretized field of the variable inside $\|\ \|$ computed over all the

381 grid points (including the boundary points) of domain D. The accuracy of the solution ψ_k

382 obtained during the iterative process in each experiment can be evaluated by the RMS of $\varepsilon(\psi_k)$,

383 denoted and defined by

384

385      $E(\psi_k) \equiv \|\varepsilon(\psi_k)\|,$ (18)

386

387 where $\|\ \|$ is defined in (17). The accuracy to which the NBE is satisfied by ψ_k can be measured

388 by $E[N(\psi_k)]$ defined in (13).

389   Table 1 lists the values of $E(\psi_k)$ and $E[N(\psi_k)]$ for the initial guess ψ_0 ($= \psi_g$) in row 1 and

390 the optimally truncated solutions ψ_K from the four experiments in rows 2-5. As shown in row

391 2 versus row 1 of Table 1, M1a reaches the optimal truncation at $k = K = 6$ where $E[N(\psi_k)]$ is

392 reduced (from 0.120 at $k = 0$) to its minimum [$= 2.411 \times 10^{-3} < E(\nabla^2 \phi) = 3.25 \times 10^{-3}$ – the NBE

393 discretization error defined in (16)] with $E(\psi_k)$ reduced (from 2.43×10^{-2} at $k = 0$) to 4.87×10^{-4}.

394   Figure 2a shows that $E(\psi_k)$ reaches its minimum ($= 4.79\times10^{-4}$) at $k = 10$. This minimum is

395   slightly below $E(\psi_K) = 4.87\times10^{-4}$ but undetectable in real-case applications.

396   On the contrary, as shown in row 3 of Table 1 and Fig. 2b, M1b reaches the optimal

397   truncation very slowly at $k = K = 38493$ where $E[N(\psi_k)]$ is reduced to its global minimum ($=$

398   1.81×10^{-2}) with $E(\psi_k)$ reduced to 1.68×10^{-3}. Here, $E[N(\psi_k)]$ has three extremely shallow and

399   small local minima (at $k = 32408$, 38490 and 38497) not visible in Fig. 2b. These local minima

400   are detected and passed by setting $m = 3$ in (13) for M1b. Clearly M1b is less accurate and

401   much less efficient than M1a.

402   Figure 2c (or 2d) shows that M2a (or M2b) reaches the optimal truncation at $k = K = 19$ (or

403   26) where $E[N(\psi_k)]$ is reduced to its global minimum [$= 3.55\times10^{-2}$ (or 2.66×10^{-2})] with $E(\psi_k)$

404   reduced to 4.55×10^{-3} (or 2.69×10^{-3}), and $E(\psi_k)$ decreases continuously toward its minimum [$=$

405   2.45×10^{-3} (or $1.62\times\times10^{-3}$)] as k increases beyond K. Thus, M2a and M2b are less efficient and

406   much less accurate than M1a for $Ro = 0.1$.

407

408   *4.2 Results from second set of experiments*

409   For this set of experiments, ψ_t and (u_t, v_t) have the same patterns as those in Fig. 1a, and

410   ψ_g and (u_g, v_g) are similar to those in Fig. 1b, but the contour intervals of ψ_t and ψ_g are reduced

411   by 50% as L is reduced from 2000 to 1000 km with Ro increased to 0.2, so the wavering jet

412   flow is on the sub-synoptic scale. In this case, the nonlinearly balanced jet flow is still inertially

413   stable over the entire domain since $\zeta_t > -f$ everywhere as shown in Fig. 3a, but $\zeta_g < -f/2$ in the

414   two small yellow colored areas as shown in Fig. 3b, so the NBE becomes hyperbolic locally in

415   this small area and the boundary value problem in (1) is not fully well posed.

416   In this case, as shown in row 2 versus row 1 of Table 2, M1a reaches the optimal truncation

417   at $k = K = 13$ where $E[N(\psi_k)]$ is reduced (from 0.243 at $k = 0$) to its minimum [$= 5.23 \times 10^{-3}$

418   close to $E(\nabla^2 \phi) = 4.33 \times 10^{-3}$] with $E(\psi_k)$ reduced (from 4.86×10^{-2} at $k = 0$) to 1.24×10^{-3}. The

419   rapid descending processes of $E(\psi_k)$ and $E[N(\psi_k)]$ (not shown) are similar to those in Fig. 2a

420   for M1a in the first set of experiments.

421   As shown in row 3 of Table 2, M1b takes $K = 48057$ iterations to reach the optimal

422   truncation and the values of $E[N(\psi_k)]$ and $E(\psi_k)$ at $k = K$ are about four times larger than those

423   from M1a. The extremely slow descending processes of $E(\psi_k)$ and $E[N(\psi_k)]$ (not shown) are

424   similar to those in Fig. 2b for M1b in the first set of experiments. As shown in row 4 (or 5) of

425   Table 2, M2a (or M2b) reaches the optimal truncation at $k = K = 26$ (or 35) and the values of

426    $E[N(\psi_K)]$ and $E(\psi_K)$ are more than (or about) 4 times of those from M1a. Thus, M1a is still

427   more accurate and much more efficient than M1b and is more efficient and much more accurate

428   than M2a and M2b for $Ro = 0.2$, although the boundary value problem in (1) in this case is not

429   fully (but nearly) well posed.

430

431   *4.3 Results from third set of experiments*

432   For this set of experiments, ψ_t and (u_t, v_t) have the same patterns as those in Fig. 1a but the

433   contour interval of ψ_t is reduced 4 times as L is reduced from 2000 to 500 km with Ro increased

434   to 0.4, so the wavering jet flow is on the meso-α scale. Figure 4a shows the fields of ψ_g and

435   (u_g, v_g) for the nonlinearly balanced jet flow. This nonlinearly balanced jet flow is inertially

436   unstable in the yellow colored area south of the ridge of wavering jet axis in the middle of

437   domain D where $\zeta_t < -f$ as shown in Fig. 4c. Figure 4d shows that $\zeta_g < -f/2$ in the long and broad

438   yellow colored area along and around the wavering jet, so the NBE is hyperbolic in this area

439   and the boundary value problem in (1) becomes seriously ill-posed.

440   In this case, as shown in row 2 of Table 3 and Fig. 5a, M1a reaches the optimal truncation

441   at $k = K = 2$ where $E[N(\psi_k)]$ is decreased (from 0.57 at $k = 0$) to its minimum (= 0.13), while

442    $E(\psi_k)$ decreases from 9.72×10^{-2} at $k = 0$ to 8.20×10^{-2} at $k = K = 2$ and then to its minimum (=

443   7.38×10^{-2}) at $k = 6$. As k increases beyond 6, M1a diverges. Its optimally truncated solution ψ_K

444   is merely slightly more accurate than the initial guess ψ_0. As shown in row 3 of Table 3 and

445   Fig. 5b, M1b reaches the optimal truncation at $k = K = 10325$ where $E[N(\psi_k)]$ is decreased to

446   its global minimum (= 0.15), while $E(\psi_k)$ decreases to 8.31×10^{-2} at $k = K$ and then to its

447   minimum (= 7.68×10^{-2}) at $k = 23515$. Thus, M1b is still less accurate and much efficient than

448   M1a.

449   Figure 5c (or 5d) shows that M2a (or M2b) reaches the optimal truncation at $k = K = 26$ (or

450   29) where $E[N(\psi_k)]$ is reduced to its minimum [= 0.11 (or 0.10)], while $E(\psi_k)$ is reduced to its

451   minimum [= 8.24×10^{-2} (or 8.24×10^{-2})] at $k = 25$ (or 26) and then increases slightly to 8.25×10^{-2}

452   ^{2} (or 8.26×10^{-2}) at $k = K = 26$ (or 29). As shown in row 4 (or 5) versus row 2 of Table 3, $E(\psi_K)$

453   from M2a (or M2b) is larger than that from M1a, so M2a (or M2b) is still less accurate than

454   M1a in this case.

455   Figure 6a (or 6b) shows that $\varepsilon(\psi_K)$ from M1a (or M1b) peaks positively and negatively in

456   the middle of domain D as $\varepsilon(\psi_0)$ does in Fig. 4b but with slightly reduced amplitudes. Figure

457   6c (or 6d) shows that $\varepsilon(\psi_K)$ from M2a (or M2b) has a broad negative peak south of the ridge

458   of wavering jet axis similar to that of $\varepsilon(\psi_0)$ in Fig. 4b but with a slightly enhanced amplitude.

21

459   In this case, M1a is still slightly more accurate than other three iterative procedures but it cannot

460   effectively reduce the solution error in the central part of the domain where not only the NBE

461   is hyperbolic (with $\zeta_g < -f/2$ as shown in Fig. 4d) but also the jet flow is strongly anti-

462   cyclonically curved and subject to inertial instability (with $\zeta_t < -f$ as shown in Fig. 4c).

463

464   *4.4 Results from fourth set of experiments*

465   For this set of experiments, ψ_t and (u_t, v_t) are plotted in Fig. 7a. These fields represent the

466   same nonlinearly balanced wavering westerly jet flow as that in the third set of experiments

467   except that the wave fields are shifted by a half of wavelength so the jet flow is curved

468   cyclonically in the middle of domain D. In this case, ψ_g and (u_g, v_g) are nearly the same as the

469   half-wavelength shifted fields (not shown) from Fig. 4a but with small differences mainly along

470   and around the trough and ridge lines due to the boundary condition, $\phi \equiv f\psi_g = f\psi_t$, used here

471   along the two trough lines (instead of the two ridge lines in Fig. 4a) for solving ϕ from $\nabla^2 \phi =$

472    $N(\psi_t)$. Figure 7c shows the jet flow becomes inertially unstable in the two yellow colored areas

473   (where $\zeta_t < -f$) around the west and east boundaries of domain D. Figure 7d shows that the NBE

474   becomes hyperbolic in the long and broad yellow colored area (where $\zeta_g < -f/2$) that is nearly

475   the same as the yellow colored area in Fig. 4d but half-wavelength shifted, so the area of $\zeta_g <$

476    $-f$ (that is, the area of $\zeta_0 + f < 0$ in which the initial guess field is inertially unstable) in Fig. 4d

477   is moved with the ridge line to the west and east boundaries in Fig. 7d. As the area of $\zeta_g < -f$

478   and area of $\zeta_t < -f$ are moved away from the domain center to the domain boundaries where ψ_t

479   is known and given by ϕ/f, solving the NBE becomes less difficult in this fourth set of

480   experiments than in the third set.

481   In this case, as shown in row 2 of Table 4 and Fig. 8a, M1a reaches the optimal truncation

482   at $k = K = 7$ where $E[N(\psi_k)]$ is decreased (from 0.76 at $k = 0$) to its minimum ($= 3.81 \times 10^{-2}$),

483   while $E(\psi_k)$ decreases from 9.71×10^{-2} at $k = 0$ to 2.29×10^{-2} at $k = K = 7$ and then to its flat

484   minimum ($= 2.25 \times 10^{-2}$) at $k = 12$, so ψ_K is significantly more accurate than ψ_0 and slightly less

485   accurate than ψ_k at $k = 12$ (which is undetectable in real-case applications). As shown in row 3

486   of Table 4 and Fig. 8b, M1b reaches the optimal truncation at $k = K = 31830$ where $E[N(\psi_k)]$

487   is decreased to its global minimum ($= 4.54 \times 10^{-2}$), while $E(\psi_k)$ decreases to 2.37×10^{-2} at $k = K$

488   and then to its minimum ($= 2.21 \times 10^{-2}$) at $k = 57586$. Thus, M1b is still much less efficient and

489   less accurate than M1a.

490   Figure 8c (or 8d) shows that M2a (or M2b) reaches the optimal truncation at $k = K = 27$ (or

491   32) where $E[N(\psi_k)]$ is reduced to its minimum [$= 5.42 \times 10^{-2}$ (or 4.66×10^{-2})], $E(\psi_k)$ reduces to

492   3.03×10^{-2} (or 2.64×10^{-2}) at $k = K$ and then to its minimum [$= 2.72 \times 10^{-2}$ (or 2.43×10^{-2})] at $k =$

493   36 (or 44), so M2a (or M2b) is still less efficient and less accurate than M1a in this case.

494   Figure 7b shows that $\varepsilon(\psi_0)$ has a broad positive (or negative) peak south (or north) of the

495   trough of wavering jet axis in the middle of domain D. These broad peaks are mostly reduced

496   by M1a as shown by $\varepsilon(\psi_K)$ in Fig. 9a but slightly less reduced by M1b as shown in Fig. 9b and

497   less reduced by M2a (or M2b) as shown in Fig. 9c (or 9d). However, the small secondary

498   negative peak of $\varepsilon(\psi_g)$ near the west (or east) boundary in Fig. 7b is reduced only about 30%

499   by M1a (or M1b) as shown by $\varepsilon(\psi_K)$ in Fig. 9a (or 9b) and even less reduced by M2a (or M2b)

500   as shown in Fig. 9c (or 9d). Thus, all the four iterative procedures have difficulties to reduce

501   the errors of their optimally truncated solutions near the west and east boundaries where not

502   only the NBE is hyperbolic (with $\zeta_g < -f/2$ as shown in Fig. 7d) but also the jet flow is subject

503   to inertial instability (with $\zeta_t < -f$ as shown in Fig. 7c). Nevertheless, since the area of $\zeta_t < -f$ is

504   moved with the ridge of wavering jet axis to the domain boundaries in Fig. 7c, all the four

505   iterative procedures perform significantly better in this set of experiments than in the previous

506   third set, as shown in Fig. 9 and Table 4 versus Fig. 6 and Table 3. In this case, M1a is still

507   most accurate and M1b is still least efficient among the four iterative procedures.

508

509   **5. Conclusions**

510   In this paper, two types of previous iterative methods for solving the NBE are reviewed and

511   revisited. The first type was originally proposed by Bolin (1955), in which the NBE is

512   transformed into a linearized equation for a presumably small correction to the initial guess or

513   the subsequently updated solution. The second type was originally proposed by Shuman (1955,

514   1957) and Miyakoda (1956), in which the NBE is rearranged into a quadratic form of the

515   absolute vorticity and the positive root of this quadratic form is used in the form of Poisson

516   equation to obtain the solution iteratively. These two types of methods are re-derived formally

517   by expanding the solution asymptotically upon a small Rossby number (see section 2), and the

518   re-derived methods are called method-1 and method-2, respectively.

519   Since the rearranged asymptotic expansion is not ensured to converge especially when the

520   Rossby number is not sufficiently small, a criterion for optimal truncation of asymptotic

521   expansion is proposed [see (13)] to obtain the super-asymptotic approximation of the solution

522   based on the heuristic theory of asymptotic analysis (Boyd, 1999). In addition, the Poisson

523   solver based on the integral formulas (Xu et al., 2011; Cao and Xu, 2011) is used versus the

524   SOR scheme to solve the boundary value problem in each iterative step.

525   The four iterative procedures are tested with analytically formulated wavering jet flows on

526   different spatial scales in four sets of experiments. The computational domain covers one full

527   wavelength and is centered at the ridge of the wavering jet in the first three sets of experiments

528   but centered at the trough in the last set. In the first set of experiments, the wavering jet flow is

529   formulated on the synoptic scale [with the half wavelength $L = 2000$ km and the associated

530   Rossby number $Ro = 0.1$]. In this case, the NBE is of the elliptic type over the entire domain

531   and therefore its boundary value problem is well posed. In the second set of experiments, the

532   wavering jet flow is formulated on the sub-synoptic scale [with $L = 1000$ km and $Ro = 0.2$]. In

533   this case, the NBE is of the elliptic type nearly over the entire domain so that its boundary value

534   problem is nearly well posed. In the third (or fourth) set of experiments, the wavering jet flow

535   is formulated on the meso-α scale with $Ro = 0.4$, the wavering jet flow is curved anti-

536   cyclonically (or cyclonically) in the middle of the domain where the absolute vorticity is locally

537   negative (or strongly positive), and the NBE becomes hyperbolic broadly along and around the

538   wavering jet so that its boundary value problem is seriously ill-posed.

539   The test results can be summarized as follows: For wavering jet flows on the synoptic and

540   sub-synoptic scales, all the four iterative procedures can reach their respective optimal

541   truncations and the solution error (originally from the initial guess – the geostrophic

542   streamfunction) can be reduced at the optimal truncation by an order of magnitude or nearly so

543   even when the NBE is not entirely elliptic. Among the four iterative procedures, M1a is most

544　accurate and efficient while M1b is least efficient. The results for wavering jet flows on the

545　synoptic and sub-synoptic scales are insensitive to the location of wavering jet in the

546　computational domain. In particular, according to our additional experiments (not shown in

547　this paper), when the wavering jet is shifted zonally by a half of wavelength (with the trough

548　moved to the domain center), the solution errors become slightly smaller and the optimal

549　truncation numbers for M1a and M1b (or M2a and M2b) become slightly smaller (or larger)

550　than those listed in Tables 1 and 2. For wavering jet flows on the meso-α scale in which the

551　NBE's boundary value problem is seriously ill-posed, the four iterative procedures still can

552　reach their respective optimal truncations with the solution error reduced effectively for

553　cyclonically curved part of the wavering jet flow but not for the anti-cyclonically curved part.

554　In this case, M1a is still most accurate and efficient while M1b is least efficient.

555　　　In comparison with M1b, the high accuracy and efficiency of M1a can be explained by the

556　fact that the solution obtained by the Poisson solver based on the integral formulas is not only

557　more accurate but also smoother than the solution obtained by the SOR scheme in each step of

558　nonlinear iteration. Consequently, in each next step, the nonlinear differential term on the right-

559　hand side of the incremental-form iteration equation [see (9a)] is computed more accurately in

560　M1a than in M1b and so is the entire right-hand side. This is especially true and important

561　when the entire right-hand side becomes very small (toward zero) in the late stage of iterations,

562　as it also explains why M1b reaches the optimal truncation much slower than M1a (see Tables

563　1–4). In comparison with M2a and M2b, the high accuracy and efficiency of M1a can be

564　explained by the fact that the solution in M1a is updated incrementally and the increment is

565   small relative to the entire solution and so is the error of the increment computed in each step

566   of nonlinear iteration. On the other hand, the solution in M2a or M2b is updated entirely and

567   the entire solution is large relative to the increment and so is the error of the entire solution

568   computed in each step of nonlinear iteration. Moreover, the recursive form of equation [see

569   (12)] used by M2a and M2b contains a square root term on its right-hand side, so it cannot be

570   converted into an incremental form. Furthermore, this square root term must set to zero when

571   the term inside the square root becomes negative, although the term inside the square root

572   corresponds to the squared absolute vorticity. This problem is caused by the non-negative

573   absolute vorticity assumed in the derivation of the recursive form of equation for M2a and M2b.

574   Cyclonically curved meso-α scale jet flows in the middle and upper troposphere are often

575   precursors of severe weather especially when the curved jet flow evolves into a cut-off cyclone

576   atop a meso-α scale low pressure system in the lower troposphere. In this case, M1a can be

577   potentially and particularly useful for severe weather analyses in the context of semi-balanced

578   dynamics (Xu, 1994; Xu and Cao, 2012). In addition, since the mass fields can be estimated

579   from Advanced Microwave Sounding Unit (AMSU) observations, using the NBE to retrieve

580   the horizontal winds in and around tropical cyclones (TC) from the estimated mass fields have

581   potentially important applications for TC warnings and improving TC initial conditions in

582   numerical predictions (Velden and Smith, 1983; Bessho et al, 2006). Applications of M1a in

583   the aforementioned directions deserve continued studies. In particular, the gradient wind can

584   be easily computed for the axi-symmetric part of a cut-off cyclone (or TC) and used to improve

585   the initial guess for the iterative procedure. This use of gradient wind can be somewhat similar

586 to the use of gradient wind associated with the axisymmetric part of a hurricane to improve the

587 basic-state potential vorticity (PV) construction for hurricane PV diagnoses (Wang and Zhang,

588 2003; Kieu and Zhang, 2010). Furthermore, either the gradient wind or the optimal truncated

589 solution from M1a can be used as a new improved initial guess. In this case, the asymptotic

590 expansion can be reformulated upon a new small parameter associated with the reduced error

591 of the new initial guess and this new small parameter can be smaller or much smaller than the

592 Rossby number used for the asymptotic expansion in this paper. The reformulated asymptotic

593 expansion may be truncated to yield a more accurate 'hyperasymptotic' approximation of the

594 solution according to the heuristic theory of asymptotic analysis (see section 5 of Boyd, 1999).

595 This approach deserves further explorations.

596

605

606   **REFERENCES**

607   Arnason, G., 1958: A convergent method for solving the balance equation. *J. Meteor.*, **15**, 220-

608   225.

609   Asselin, R., 1967: The operational use of the balance equation. *Tellus*, **19**, 24-32.

610   Bessho, K., M. Demaria, and J. Knaff, 2006: Tropical cyclone wind retrievals from the

611   advanced microwave sounding unit: application to surface wind analysis. *J. Appl. Meteor.*,

612   **45**, 399-415.

613   Bijlsma, S., and R. Hoogendoorn, 1983: A convergence analysis of a numerical method for

614   solving the balance equation. *Mon. Wea. Rev.*, **111**, 997-1001.

615   Bolin, B., 1955: Numerical forecasting with the barotropic model. *Tellus*, **7**, 27-49.

616   Bolin, B., 1956: An improved barotropic model and some aspects of using the balance equation

617   for three-dimensional flow. *Tellus*, **8**, 61-75.

618   Boyd, J. P., 1999: The devil's invention: Asymptotic, superasymptotic and hyperasymptotic

619   series. *Acta Applicandae Mathematicae*, **56**, 1–98.

620   Bring, A., and Charasch, E., 1958: An experiment in numerical prediction with two non-

621   geostrophic barotropic models. *Tellus*, **10**, 88-94.

622   Bushby, F. H., and V. M. Huckle, 1956: The use of a stream function in a two-parameter model

623   of the atmosphere. *Quart. J. Roy. Meteor. Soc.*, **82**, No. 354, 409-418.

624   Cao, J. and Q. Xu, 2011: Computing streamfunction and velocity potential in a limited domain.

625   Part II: Numerical methods and test experiments. *Adv. Atmos. Sci.*, **28**, 1445-1458.

626   Charney, J., 1955: The use of the primitive equations of motion in numerical forecasting. *Tellus*,

627   **7**, 22-26.

628   Charney, J. G., and M. E. Stern, 1962: On the stability of internal baroclinic jets in a rotating

629   atmosphere. *J. Atmos. Sci.*, **19**, 159-172.

630   Courant, R., and D. Hilbert, 1962: *Methods of Mathematical Physics*. Vol. II. Interscience, 830

631   pp.

632   Kieu, C. Q., and D.-L. Zhang, 2010: A piecewise potential vorticity inversion algorithm and

633   its application to hurricane inner-core anomalies. J. Atmos. Sci., 67, 1745-1758.

634   Kuo, H. L., 1959: Finite amplitude three-dimensional harmonic waves on the spherical earth.

635   *J. Meteor.*, **16**, 524-534.

636   Liao, T., and T. Chow, 1962: On the method for solving the balance equation in finite difference

637   form. *Acta Meteor. Sinica*, 32, 224-231.

638   Miyakoda, K., 1956: On a method of solving the balance equation. *J. Meteor. Soc. Japan*, **34**,

639   364-367.

640   Schubert, W. H., R. K. Taft, and L. G. Silvers, 2009: Shallow water quasi-geostrophic theory

641   on the sphere. *J. Adv. Model. Earth Syst.*, **1**, No. 2, 1-17.

642   Shuman, F. G., 1955: A method for solving the balance equation. *Technical Memorandum* No.

643   6, Joint Numerical Weather Prediction Unit, 12 pp.

644   Shuman, F. G., 1957: Numerical methods in weather prediction: I. The balance equation. *Mon.*

645   *Wea. Rev.*, **85**, 329–332.

646   Southwell, R. V., 1946: *Relaxation Methods in Theoretical Physics*. Oxford, Clarendon Press,

647   248 pp.

648   Velden, C. S., and W. L. Smith, 1983: Monitoring tropical cyclone evolution with NOAA

649   satellite microwave observations. *J. Appl. Meteor.*, **22**, 714–724.

650   Wang, X., and D-L. Zhang, 2003: Potential vorticity diagnosis of a simulated hurricane. Part

651   I: Formulation and quasi-balanced flow. *J. Atmos. Sci.*, **60**, 1593-1607.

652   Xu, Q., 1994: Semibalance model—connection between geostrophic-type and balanced-type

653   intermediate models. *J. Atmos. Sci.*, **51**, 953-970.

654   Xu, Q., and J. Cao, 2012: Semibalance model in terrain-following coordinates. *J. Atmos. Sci.*,

655   **69**, 2201–2206.

656   Xu, Q., J. Cao, and S. Gao, 2011: Computing streamfunction and velocity potential in a limited

657   domain. Part I: Theory and integral formulae. *Adv. Atmos. Sci.*, **28**, 1433-1444.

658   Zhu, T., D-L. Zhang, and F. Weng, 2002: Impact of the advanced microwave sounding unit

659   measurements on hurricane prediction. *Mon. Wea. Rev.*, **130**, 2416-2432.

660

661 Table 1. Values of $E(\psi_k)$ and $E[N(\psi_k)]$ listed in row 1 for the initial guess ψ_0 ($= \psi_g$) with $k = 0$

662 and in rows 2-5 for ψ_K from the four iterative procedures in the first set of experiments (with

663 $Ro = 0.1$). Here, $E(\psi_k)$ is defined in (18), $E[N(\psi_k)]$ is defined in (13), k is the iteration number,

664 and ψ_K is the optimally truncated solution at $k = K$.

	$E(\psi_k)$	$E[N(\psi_k)]$	k
ψ_0	2.43×10^{-2}	0.120	$k = 0$
M1a	4.87×10^{-4}	2.41×10^{-3}	$k = K = 6$
M1b	1.68×10^{-3}	1.81×10^{-2}	$k = K = 38493$
M2a	4.55×10^{-3}	3.55×10^{-2}	$k = K = 19$
M2b	2.69×10^{-3}	2.66×10^{-2}	$k = K = 26$

665

666 Table 2. As in Table 1 but for the second set of experiments (with $Ro = 0.2$).

	$E(\psi_k)$	$E[N(\psi_k)]$	k
ψ_0	4.86×10^{-2}	0.243	$k = 0$
M1a	1.24×10^{-3}	5.23×10^{-3}	$k = K = 13$
M1b	5.14×10^{-3}	2.20×10^{-2}	$k = K = 48057$
M2a	6.31×10^{-3}	4.17×10^{-2}	$k = K = 26$
M2b	3.96×10^{-3}	2.94×10^{-2}	$k = K = 35$

667

668 Table 3. As in Table 1 but for the third set of experiments (with $Ro = 0.4$ and $x_0 = 0$).

	$E(\psi_k)$	$E[N(\psi_k)]$	k
ψ_0	9.72×10^{-2}	0.57	$k = 0$
M1a	8.20×10^{-2}	0.13	$k = K = 2$
M1b	8.31×10^{-2}	0.15	$k = K = 10325$
M2a	8.25×10^{-2}	0.11	$k = K = 26$
M2b	8.26×10^{-2}	0.10	$k = K = 29$

669

670 Table 4. As in Table 1 but for the fourth set of experiments (with $Ro = 0.4$ and $x_0 = L$).

	$E(\psi_k)$	$E[N(\psi_k)]$	k
ψ_0	9.71×10^{-2}	0.76	$k = 0$
M1a	2.29×10^{-2}	3.81×10^{-2}	$k = K = 7$
M1b	2.37×10^{-2}	4.54×10^{-2}	$k = K = 31830$
M2a	3.03×10^{-2}	5.42×10^{-2}	$k = K = 27$
M2b	2.64×10^{-2}	4.66×10^{-2}	$k = K = 32$

671
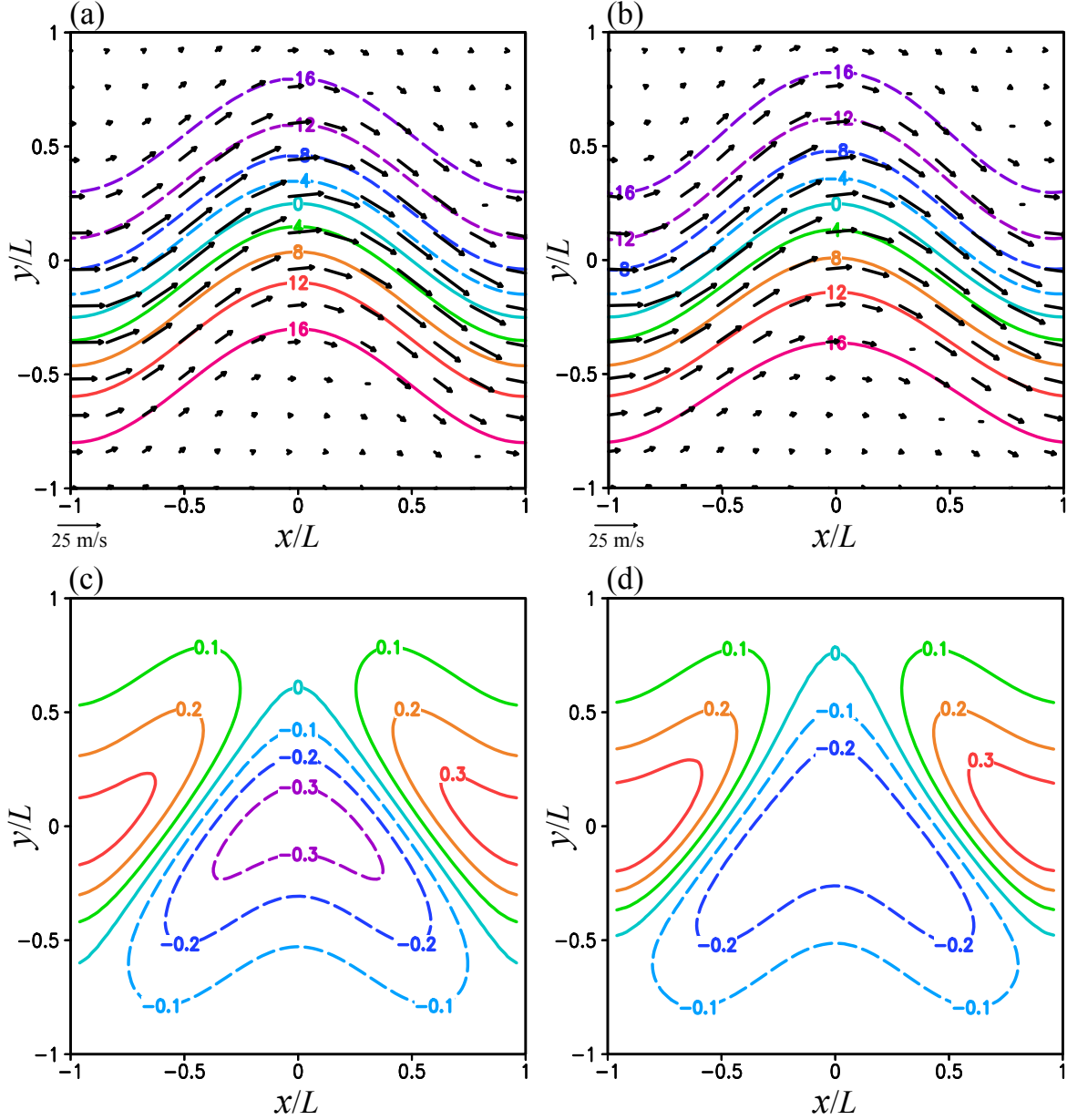
Fig. 1. (a) ψ_t plotted by color contours every 4.0 in the unit of 10^6 m²s⁻¹ and (u_t, v_t) plotted by black arrows over domain $D \equiv [-L \leq x \leq L, -L \leq y \leq L]$ with $L = 2000$ km for the first set of experiments. (b) As in (a) but for ψ_g and (u_g, v_g) with $\psi_g \equiv \phi/f$ and ϕ computed from ψ_t by setting $f = f_o = 10^{-4}$ s⁻¹ as described in section 3.3. (c) Vorticity $\zeta_t \equiv \nabla^2 \psi_t$ plotted by color contours every 0.1 in the unit of 10^{-4} s⁻¹ over domain D. (d) As in (c) but for geostrophic vorticity $\zeta_g \equiv \nabla^2 \psi_g$. The wavering jet axis is along the green contour of $\psi_t = 0$ in (a) with its ridge at $x = 0$ and two troughs at $x = \pm L$ on the west and east boundaries of domain D.

33
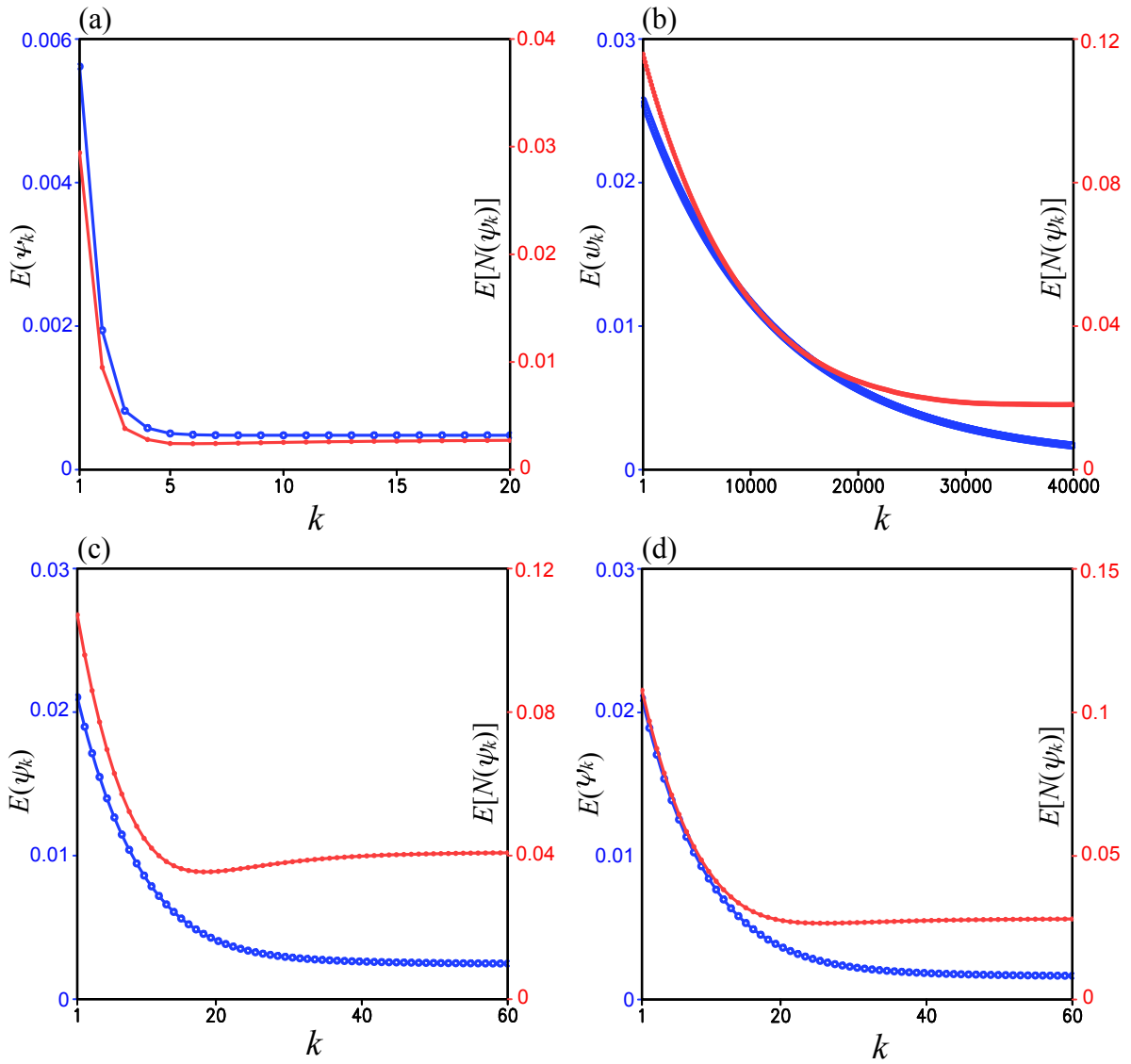
Fig. 2. (a) $E[N(\psi_k)]$ and $E(\psi_k)$ from M1a in the first set of experiments plotted by red and blue

curves, respectively, as functions of k over the range of $1 \leq k \leq 20$. (b) As in (a) but from M1b

plotted over the range of $1 \leq k \leq 4 \times 10^4$. (c) As in (a) but from M2a plotted over the range of 1

$\leq k \leq 60$. (d) As in (c) but from M2b. In each panel, the ordinate of $E[N(\psi_k)]$ is on the left side

labeled in red and the ordinate of $E(\psi_k)$ is on the right side labeled in blue.

689
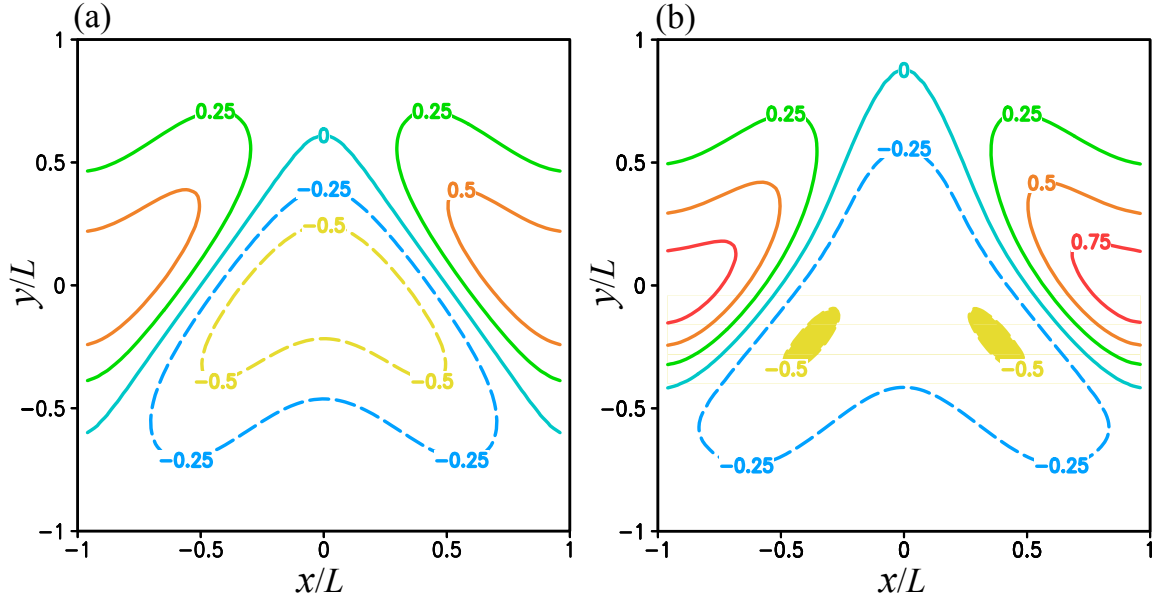
Fig. 3. (a) ζ_t plotted by color contours every 0.25 in the unit of 10^{-4} s^{-1} in domain D with $L = 1000$ km and $Ro = 0.2$ for the second set of experiments . (b) As in (a) but for ζ_g. As shown in (b), $\zeta_g < -f/2$ (= $-f_o/2$) in the two small yellow colored areas where the NBE becomes locally hyperbolic.
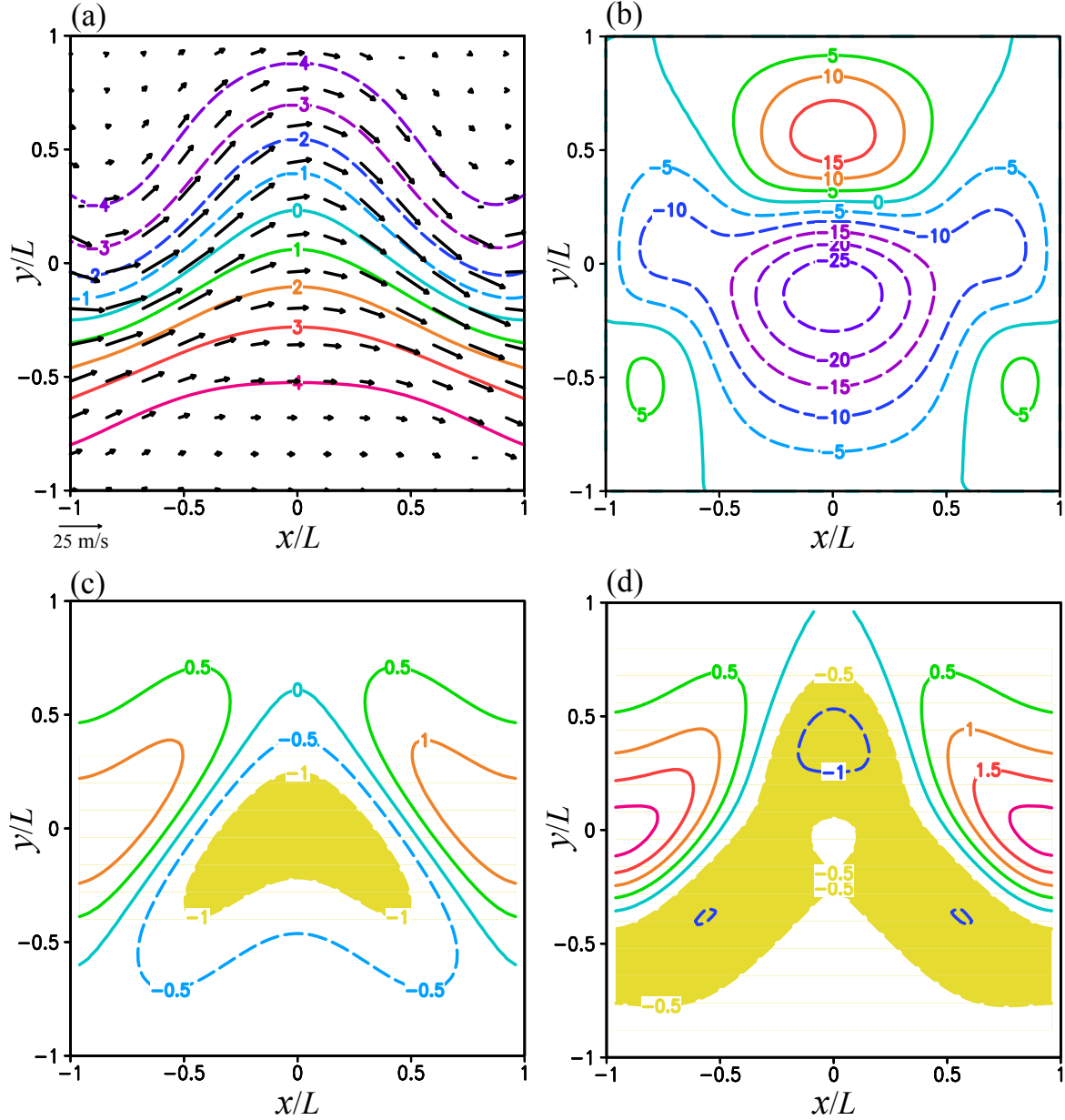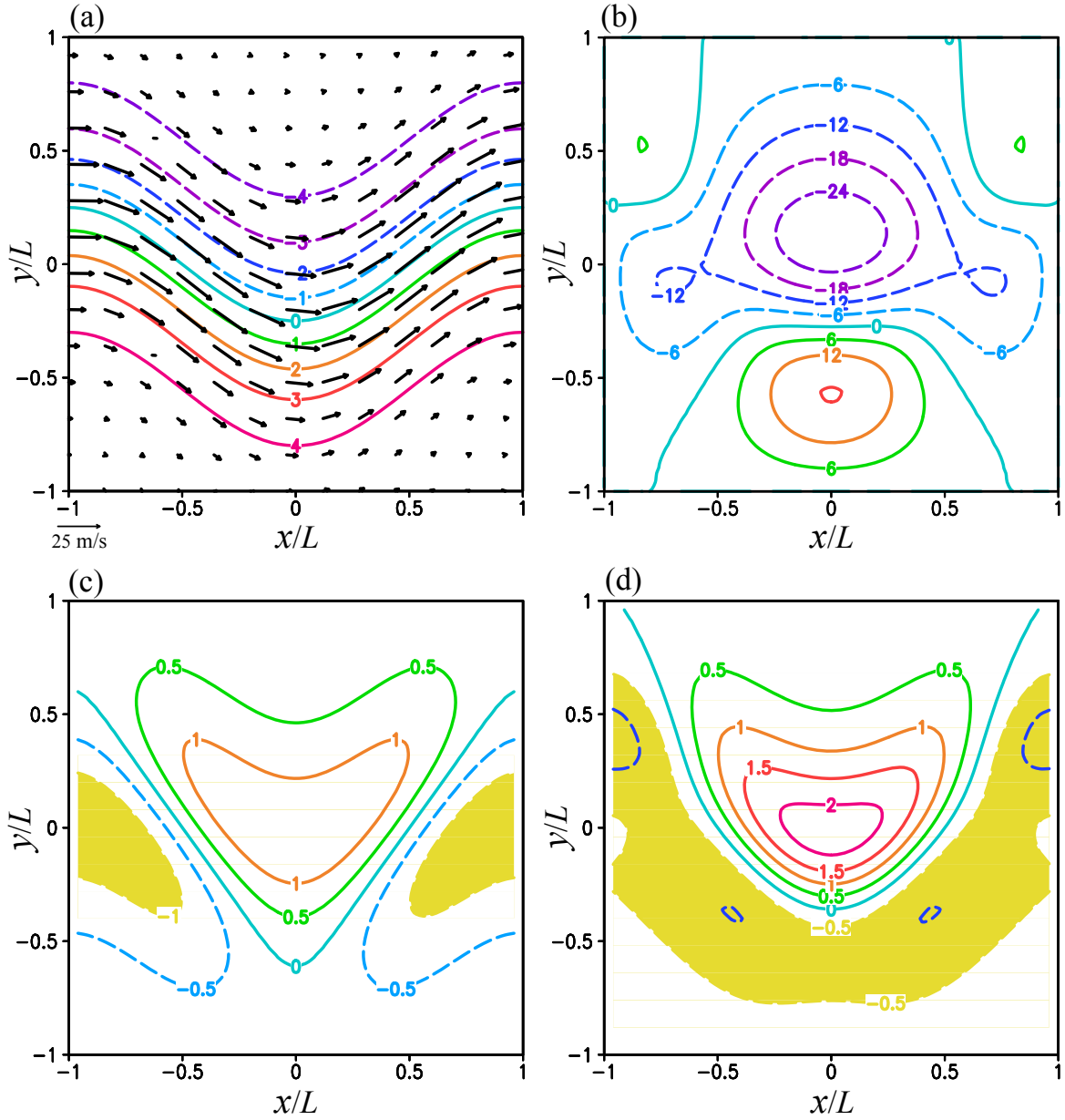
Fig. 4. (a) ψ_g plotted by color contours every 1.0 in the unit of 10^6 m^{2}s^{-1} and (u_g, v_g) plotted by black arrows over domain D with $L = 500$ km and $Ro = 0.4$ for the third set of experiments. (b) As in (a) but for $\varepsilon(\psi_0) = \varepsilon(\psi_g)$ plotted by color contours every 5.0 in the unit of 10^{-2}. (c) As in (a) but for ζ_t plotted by color contours every 0.5 in the unit of 10^{-4} s^{-1} in domain D. (d) As in (c) but for ζ_g. As shown in (c), $\zeta_t < -f$ in the yellow colored area south of the ridge of wavering jet axis where the jet flow becomes inertially unstable. As shown in (c), $\zeta_g < -f/2$ $(= -f_0/2)$ in the long and broad yellow colored area (along and around the wavering jet) where the NBE becomes hyperbolic.
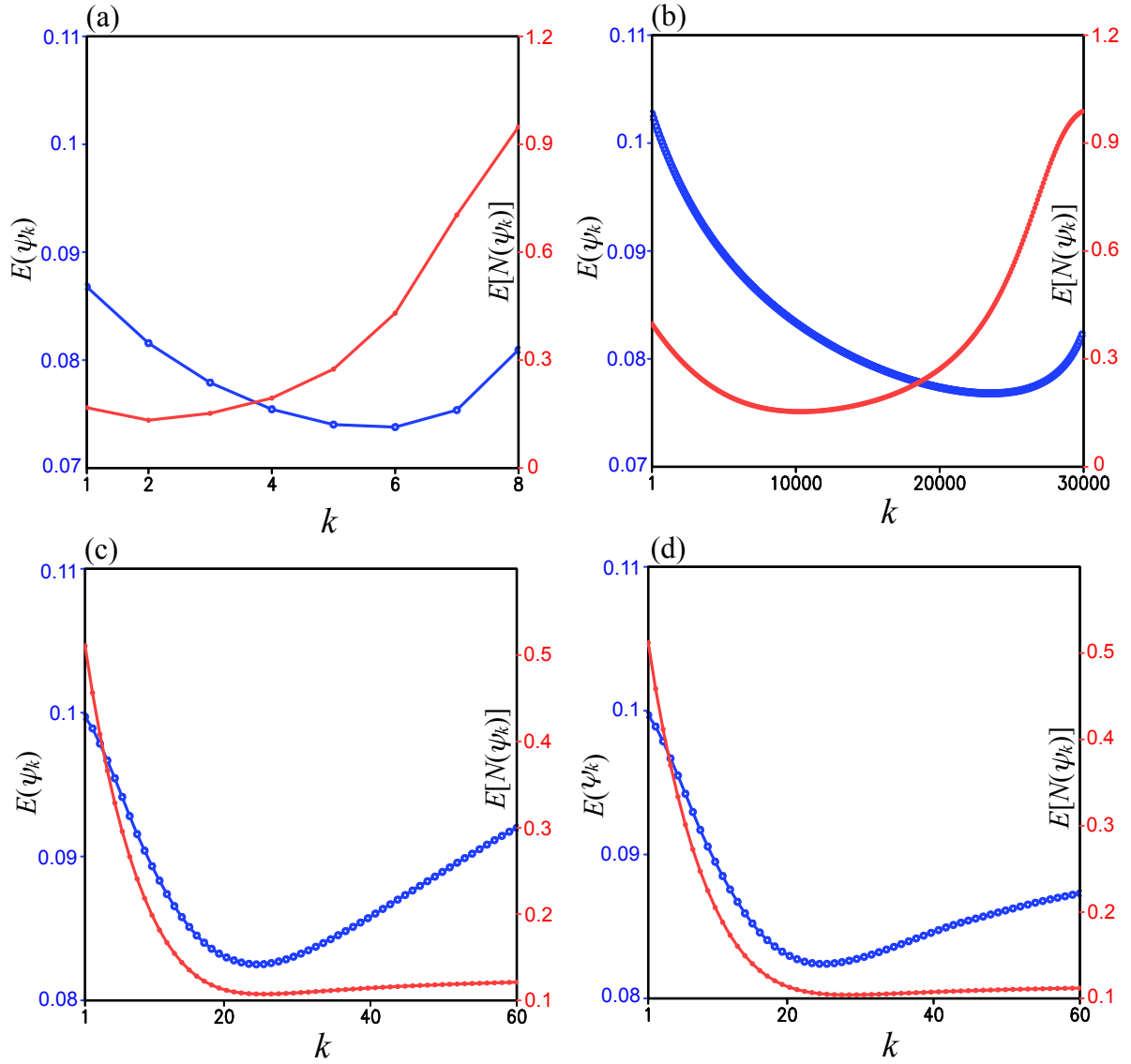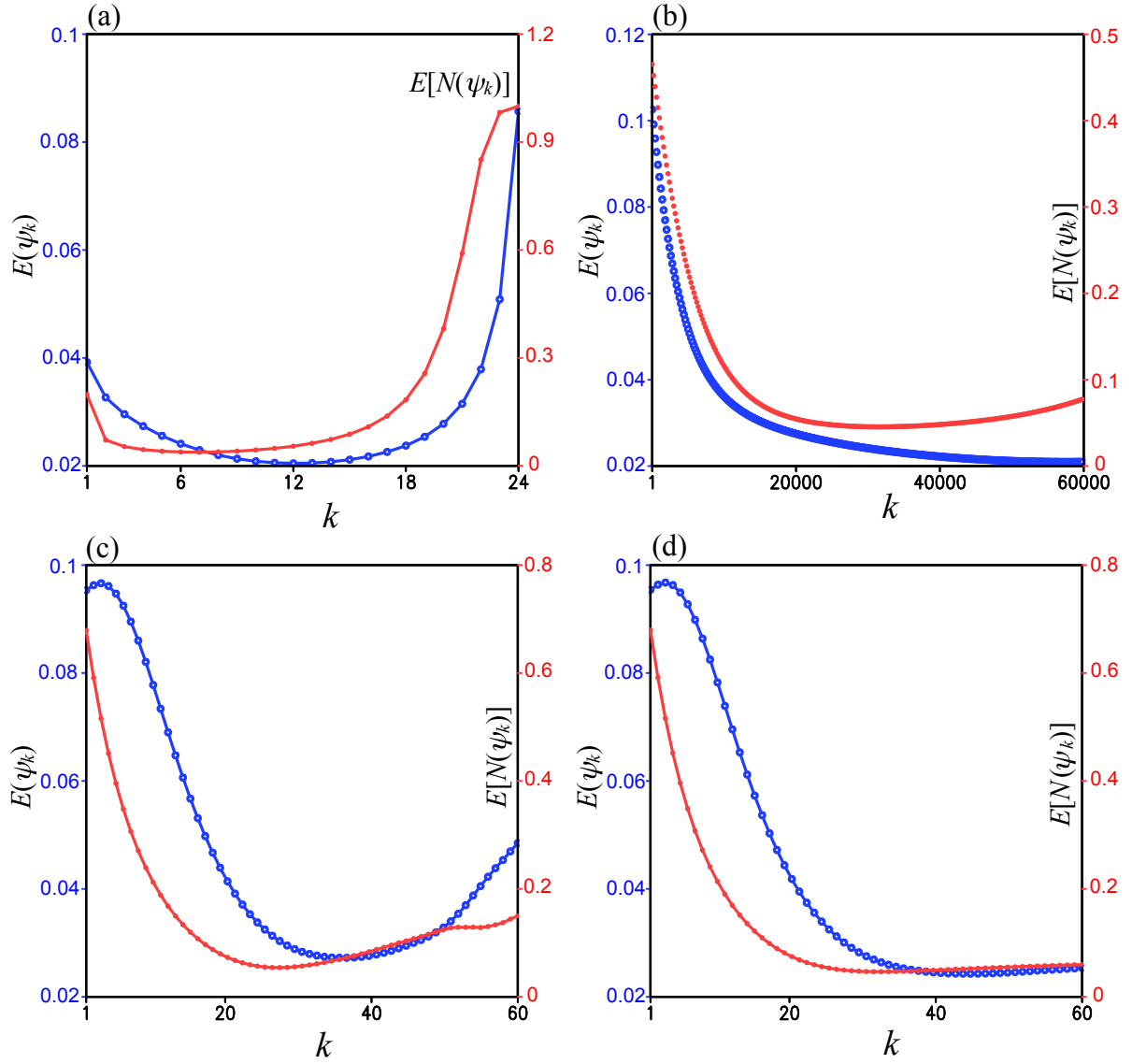
Fig. 5. (a) $E[N(\psi_k)]$ and $E(\psi_k)$ from M1a in the third set of experiments plotted by red and blue curves, respectively, as functions of k over the range of $1 \leq k \leq 8$, (b) As in (a) but from M1b plotted over the range of $1 \leq k \leq 3 \times 10^4$. (c) As in (a) but from M2a plotted over the range of $1 \leq k \leq 60$. (d) As in (a) but from M2b. In each panel, the ordinates of $E[N(\psi_k)]$ and $E(\psi_k)$ are placed and labeled as in Fig. 2.
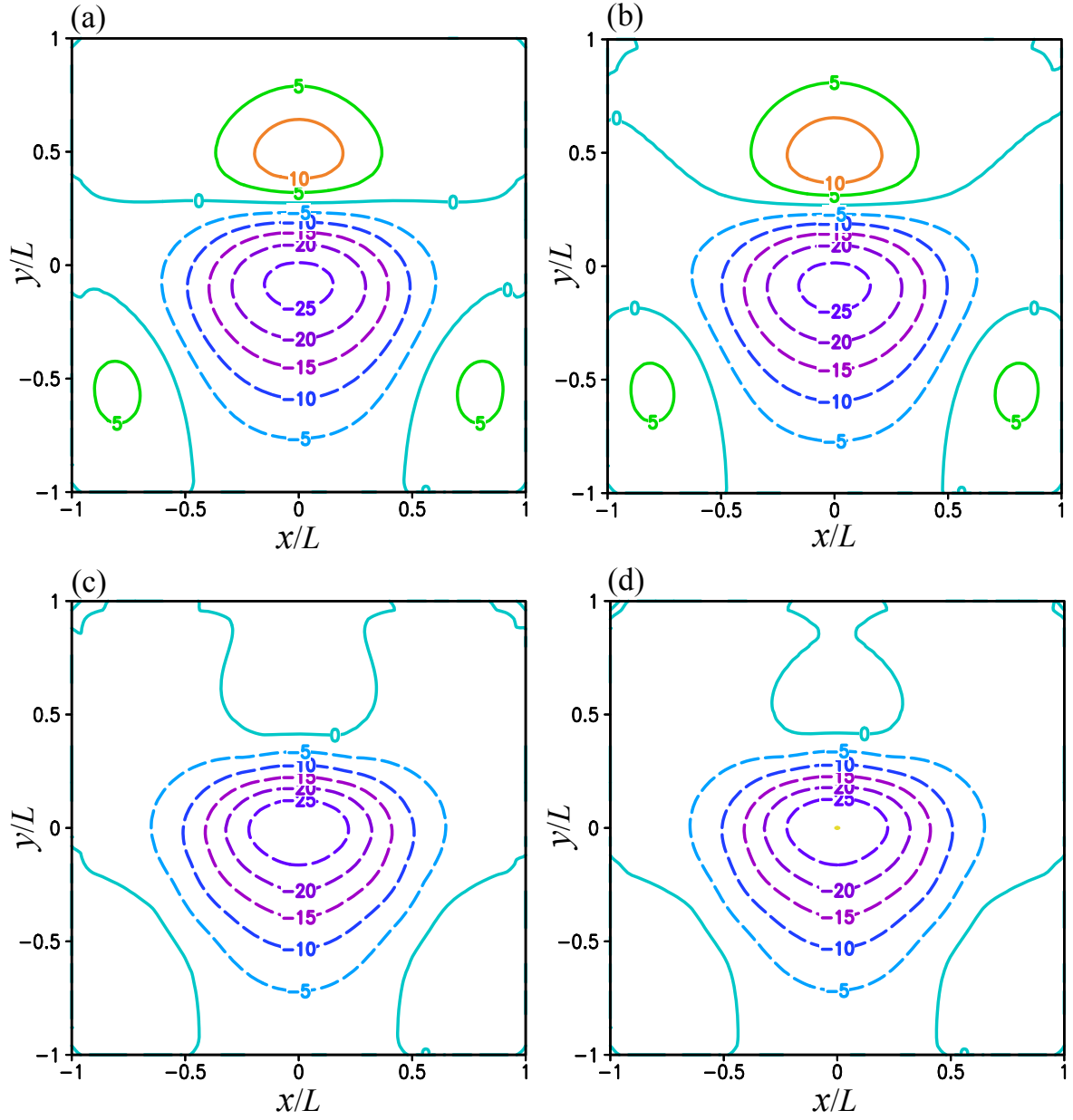
Fig. 6. $\varepsilon(\psi_K)$ plotted by color contours every 0.5 in the unit of 10^{-2} for ψ_K from (a) M1a, (b) M1b, (c) M2a and (d) M2b in the third set of experiments.

Fig. 7. (a) As in Fig. 4a but for ψ_t and (u_t, v_t) in the fourth set of experiments with $L = 500$ km and $x_0 = L$ (instead of $x_0 = 0$). (b) As in (a) but for $\varepsilon(\psi_0) = \varepsilon(\psi_g)$ plotted by color contours every 6.0 in the unit of 10^{-2}. (c) As in (a) but for ζ_t plotted by color contours every 0.5 in the unit of 10^{-4} s^{-1} in domain D. (d) As in (c) but for ζ_g.

Fig. 8. (a) $E[N(\psi_k)]$ and $E(\psi_k)$ from M1a in the fourth set of experiments plotted by red and blue curves, respectively, as functions of k over the range of $1 \leq k \leq 24$, (b) As in (a) but from M1b plotted over the range of $1 \leq k \leq 6 \times 10^4$. (c) As in (a) but from M2a plotted over the range of $0 \leq k \leq 60$. (d) As in (a) but from M2b. In each panel, the ordinates of $E[N(\psi_k)]$ and $E(\psi_k)$ are placed and labeled as in Fig. 2.
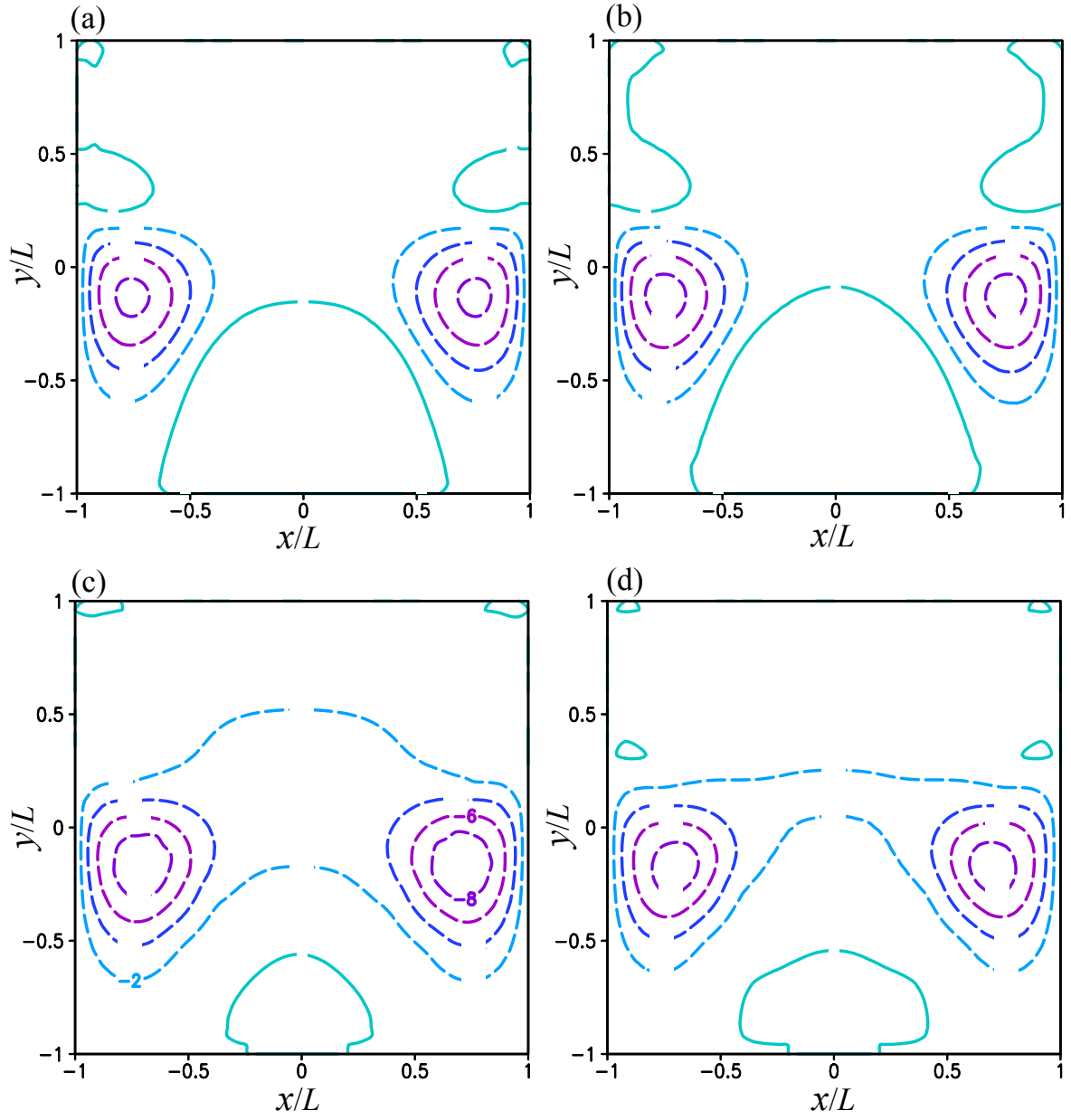
Fig. 9. $\varepsilon(\psi_K)$ plotted by color contours every 2.0 in the unit of 10^{-2} for ψ_K from (a) M1a, (b) M1b, (c) M2a and (d) M2b in the fourth set of experiments.